

Repeated constrained sparse coding with partial dictionaries for hyperspectral unmixing

Naveed Akhtar, Faisal Sahfait and Ajmal Mian
The University of Western Australia
WA, 35 Stirling Highway, Crawley, 6009

21256204@students.uwa.edu.au, faisal.shafait@uwa.edu.au, ajmal.mian@uwa.edu.au

Abstract

Hyperspectral images obtained from remote sensing platforms have limited spatial resolution. Thus, each spectra measured at a pixel is usually a mixture of many pure spectral signatures (endmembers) corresponding to different materials on the ground. Hyperspectral unmixing aims at separating these mixed spectra into its constituent endmembers. We formulate hyperspectral unmixing as a constrained sparse coding (CSC) problem where unmixing is performed with the help of a library of pure spectral signatures under positivity and summation constraints. We propose two different methods that perform CSC repeatedly over the hyperspectral data. However, the first method, Repeated-CSC (RCSC), systematically neglects a few spectral bands of the data each time it performs the sparse coding. Whereas the second method, Repeated Spectral Derivative (RSD), takes the spectral derivative of the data before the sparse coding stage. The spectral derivative is taken such that it is not operated on a few selected bands. Experiments on simulated and real hyperspectral data and comparison with existing state of the art show that the proposed methods achieve significantly higher accuracy. Our results demonstrate the overall robustness of RCSC to noise and better performance of RSD at high signal to noise ratio.

1. Introduction

Modern remote sensing instruments such as the NASA's Airborne Visible Infrared Imaging Spectrometer (AVIRIS) [10] take hyperspectral (HS) images of Earth for geological studies. These images can be represented as HS cubes with two spatial and one spectral dimension (see Fig. 1). In typical remote sensing HS images, the spectral dimension consists of hundreds of contiguous bands in the visible and short infrared wavelength range. However, each pixel of the image cube represents a large area of the Earth's surface in the spatial dimensions [4]. For instance, in the

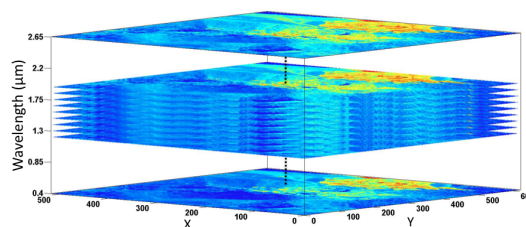


Figure 1: Illustration of hyperspectral image cube. The cube shows only eleven spectral bands (out of 224 bands) captured by AVIRIS. The image is taken over Cuprite mines, Nevada.

images captured by EnMAP HS imager of Germany [1] and Hyperion of NASA [17], each pixel represents about $30m^2$ area on the ground. Due to the low spatial resolution of HS sensors, the spectra measured by a sensor pixel is usually a mixture of spectra of different pure materials on the ground. Each spectra of pure material is called an *endmember*. Hyperspectral unmixing is the process of separating the measured spectra into its constituent endmembers and a set of *fractional abundances* of the corresponding materials (i.e. the proportion of each material in the image pixel), one set per pixel [5].

Hyperspectral unmixing is an active research area in remote sensing community [3], where it is seen as a blind source separation problem with the sources being statistically dependent [14]. Many works in hyperspectral unmixing exploit geometrical properties of the data in observed mixed pixels. These approaches are mainly based on the premise that in each mixed pixel the fractional abundances form a probability simplex and among a given collection of material spectra the constituent pixel endmembers can be found by estimating the smallest simplex set containing the observed pixel spectra [21], [20]. These methods assume presence of at least one pure pixel for every material captured in the image, thus requiring *endmember extraction* algorithms [14]. Vertex component analysis [18], N-FINDER

[24], orthogonal subspace projection technique [22] and Pixel Purity Index [6] are some of the popular techniques and algorithms for endmember extraction for hyperspectral unmixing. The assumption of the existence of pure pixels in remote sensing HS cubes is not a practical one, therefore techniques like iterative error analysis [19], convex cone analysis [11], minimum volume simplex analysis [15] and minimum volume constrained non-negative matrix factorization [16] have been proposed to circumvent the problem by generating pure endmembers from hyperspectral images. However, these techniques are likely to fail in highly mixed scenarios, where the algorithms end up generating artificial endmembers that cannot be associated with spectral signatures of true materials [12].

To overcome the aforementioned issues, hyperspectral unmixing has recently been approached in a semi-supervised fashion [4], [3], [14], [13]. Under the assumption that an observed mixed pixel spectra can be represented as a linear combination of finite number of pure spectra of known materials, these approaches formulate hyperspectral unmixing as a sparse regression problem. They make use of spectral libraries of pure material made publicly available by US Geological Survey (USGS) [8] and Jet Propulsion Lab, NASA [2]. One major challenge faced by sparse regression approaches is the fact that the spectral libraries have very high mutual coherence between their elements [4], [3], [14]. Due to the large number of similar library elements (i.e. elements with high mutual coherence), a given mixed spectra can be represented with multiple different combinations of the library elements. Thus, detecting the correct linear combination of the endmembers, out of all possible linear combinations of the library elements, becomes a challenging problem. Researchers at German Aerospace Center (DLR) [4], [3] have recently proposed to increase the endmember detection rate by taking spectral derivatives of the library elements and the given HS image. Spectral derivative significantly reduces the mutual coherence of the library elements. This approach is able to increase the endmember detection rate but at the same time it is very sensitive to noise and works well only for HS images with very high Signal to Noise Ratio (SNR).

In this work we formulate hyperspectral unmixing as a constrained sparse coding problem and propose two different methods to improve the endmember detection rate. One of these methods shows better overall robustness to noise, whereas the other performs better at high SNR. In the first method, we propose to perform sparse coding of the HS cube repeatedly such that in each sparse coding step (except the first) few spectral bands in the library and the image are systematically neglected. Fractional abundances of the detected endmembers in each step are then combined in a weighted fashion. In the second method, sparse coding is again performed repeatedly. However, this time the coding

is performed on the library and the image that is obtained by taking their spectral derivatives. The spectral derivatives are taken such that they are not operated on a few selected bands of the data. We perform experiments with the proposed methods on simulated data and real HS cube obtained by AVIRIS. We compare our results with the state of the art results shown by researchers at DLR in order to evaluate our methods. Experiments show improvements in the results with the proposed methods, especially for low SNR of HS images.

This paper is organized as following: after formulating the problem in Section 2, we present the proposed methods in Section 3. Results of the experiments with the proposed methods and discussion on these results are given in Section 4. Section 5 concludes this work by summarizing the findings.

2. Problem Formulation

2.1. Linear Mixing Model

In this work, we focus on Linear Mixing Model (LMM) [5] for hyperspectral unmixing. This model assumes that at any given band in an HS cube, the spectral response of a pixel is a linear combination of all the constituent endmembers at that particular band. Written mathematically,

$$y_i = \sum_{j=1}^p l_{ij} \alpha_j + \epsilon_i \quad (1)$$

where y_i is the value of spectral reflectance measured at i^{th} spectral band, l_{ij} is the reflectance of the j^{th} endmember of the pixel at band i , α_j is the fractional abundance of the j^{th} endmember and ϵ_i is the noise affecting the measurement. Assuming that HS image is acquired by a sensor with m spectral channels, LMM can be written in a matrix form:

$$\mathbf{y} = \mathbf{L}\boldsymbol{\alpha} + \boldsymbol{\epsilon} \quad (2)$$

where $\mathbf{y} \in \mathbb{R}^{m \times 1}$ represents the measured reflectance at a pixel, $\mathbf{L} \in \mathbb{R}^{m \times p}$ is a matrix with p pure endmembers, $\boldsymbol{\alpha} \in \mathbb{R}^{p \times 1}$ is a vector with fractional abundances of the endmembers as its elements and $\boldsymbol{\epsilon} \in \mathbb{R}^{m \times 1}$ represents noise.

In a linear mixing model, fractional abundances of the constituent endmembers are subject to two constraints [5], (a) Abundance Non-negativity Constraint (ANC) ($\forall_i, i \in \{1, \dots, p\}, \alpha_i \geq 0$) and (b) Abundance Sum-to-one Constraint (ASC) ($\sum_{i=1}^p \alpha_i = 1$). These constraints owe to the fact that fractional abundances of the endmembers are non-negative quantities which, if detected exactly, sum up to 1 for the area represented by a pixel.

2.2. Hyperspectral Unmixing as Sparse Approximation

Let us denote a spectral library of materials by a matrix $\mathbf{D} \in \mathbb{R}^{m \times k}$ ($k > m$) with each column $\mathbf{d}_i \in \mathbb{R}^{m \times 1}$ representing spectra of a pure material that is normalized to l_2 unit length. If we neglect noise, under LMM the spectral measurement \mathbf{y} at any pixel of an HS image can be reconstructed with the spectral library:

$$\mathbf{y} = \mathbf{D}\boldsymbol{\alpha} \quad (3)$$

In practice, a given pixel ($30m^2$ ground area) contains only a limited number of materials. It would be safe to assume that a given sensed spectra will be a linear combination of no more than p pure spectra, where $p \ll k$. Note that, in the literature related to sparse representation of images, \mathbf{D} is referred as *dictionary* and \mathbf{d}_i is termed as its *atom*. However, here we stick to the more common naming convention of remote sensing community and refer to \mathbf{D} as a library and \mathbf{d}_i as a pure spectral signature or an endmember.

With $k > m$, (3) represents an underdetermined system of equations that can have an infinite number of solutions. Therefore, instead of solving (3) we can minimize $\|\mathbf{D}\boldsymbol{\alpha} - \mathbf{y}\|_2$, where $\|\cdot\|_2$ is the l_2 Euclidean norm. Thus, we arrive at the following sparse approximation problem for hyperspectral unmixing:

$$\min \|\boldsymbol{\alpha}\|_0 \text{ s.t. } \|\mathbf{D}\boldsymbol{\alpha} - \mathbf{y}\|_2 \leq \eta \quad (4)$$

where η is some tolerance. Solving the above mentioned equation is NP-hard. However, its polynomial time approximation can be achieved by replacing l_0 minimizer with l_1 minimizer [7]. The sparse approximation problem can thus be re-written as:

$$\min \|\boldsymbol{\alpha}\|_1 \text{ s.t. } \|\mathbf{D}\boldsymbol{\alpha} - \mathbf{y}\|_2 \leq \eta \quad (5)$$

By including the Abundance Non-negativity Constraint in the above equation we arrive at the following constraint optimization problem:

$$\min \|\boldsymbol{\alpha}\|_1 \text{ s.t. } \|\mathbf{D}\boldsymbol{\alpha} - \mathbf{y}\|_2 \leq \eta \forall i, \alpha_i \geq 0 \quad (6)$$

Equation 6 can be solved using basis pursuit (BP) algorithm [7] or LASSO (least absolute shrinkage and selection operator) [23], with positivity constraint on the sparse vector coefficients. Previous works in hyperspectral unmixing (e.g. [3], [4]) formulate the problem as in Equation 6 and manually tune the value of η to find the approximation which gives the best results. It is also possible to achieve the same results by solving the following constrained sparse coding problem instead of (6):

$$\min_{\boldsymbol{\alpha}} \|\mathbf{D}\boldsymbol{\alpha} - \mathbf{y}\|_2 \text{ s.t. } \|\boldsymbol{\alpha}\|_1 \leq \lambda, \forall i, \alpha_i \geq 0 \quad (7)$$

The main advantage of formulating the hyperspectral unmixing problem as (7) is that we can use Abundance Sum-to-one Constraint to guess the value of λ a priori.

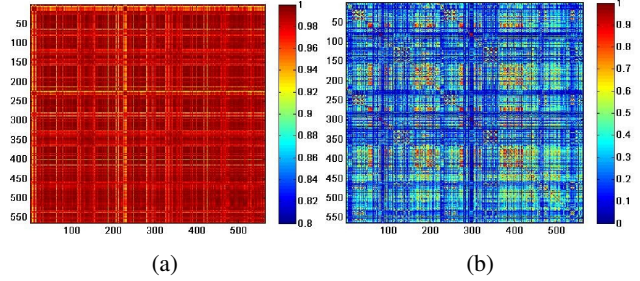


Figure 2: (a) Coherence matrix of the original library, with columns selected such that no two of them are more than 25 deg apart. (b) Coherence matrix of the differentiated library, with $c = 2$ in (9).

2.3. Mutual Coherence

Mutual coherence of a library, $\mu(\mathbf{D})$, is defined as:

$$\mu(\mathbf{D}) = \max_{i \neq j} |\mathbf{d}_i^T \cdot \mathbf{d}_j| \quad (8)$$

In sparse approximation techniques, small mutual coherence of the library is one of the most desirable conditions [3]. This is because, similar spectral signatures in the library can result in false detections of library elements in the sparse approximation process. However, in the case of large overcomplete libraries of material spectral signatures, high mutual coherence is unavoidable.

Iordache et. al. [14] show that for the value of ‘ p ’ to be as high as 10, considerable improvements can be achieved in sparse unmixing if the library is restricted to have spectral signatures that are different by 3 deg (i.e. $\mu(\mathbf{D}) \leq 0.9986$). Bieniarz et al. [3] have proposed an approach that significantly reduces $\mu(\mathbf{D})$ by taking the spectral derivative of the library. Spectral derivative of a spectral signature $\mathbf{d} \in \mathbb{R}^{m \times 1}$, is defined as:

$$\Delta(\mathbf{d}) = \frac{d(b_i) - d(b_j)}{b_j - b_i}, \forall i \in \{1, \dots, m - c\} \quad (9)$$

where, b_k is the wavelength at k^{th} band, $d(b_k)$ is the reflectance of the material at that wavelength and $j = i + c$, where $c = 1$. Fig. 2 shows an example of coherence reduction of a library using the spectral derivative. The image on the left shows the coherence matrix ($\mathbf{D}^T \mathbf{D}$) of a library with $\mu(\mathbf{D}) = 0.9$. Coherence matrix of the differentiated library is represented by the image on the right.

It should be noticed that the operation of spectral derivative is very sensitive to noise. This is because, with a high spectral resolution of a hyperspectral sensor and $c = 1$ in (9), the value of spectral derivative at a band can change drastically with a small change in the reflectance value (due to noise) at that band or its adjacent band. Without greatly

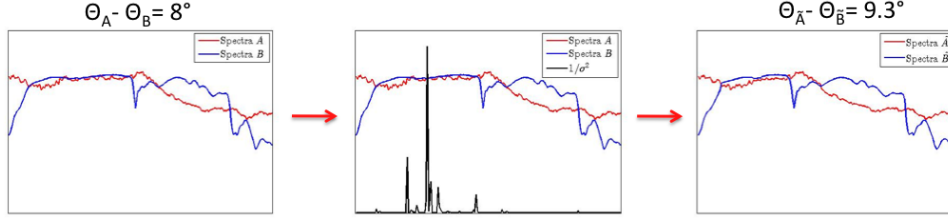


Figure 3: Coherence reduction by band removal: (Left) Spectral signatures of two materials from the USGS Library that are 8 deg apart. (Center) Peaks (in black) indicate the spectral bands at which the variance between the reflectances is very low. (Right) Spectral signatures after removal of 25 bands with lowest variance. The signatures are 9.3 deg apart after band removal.

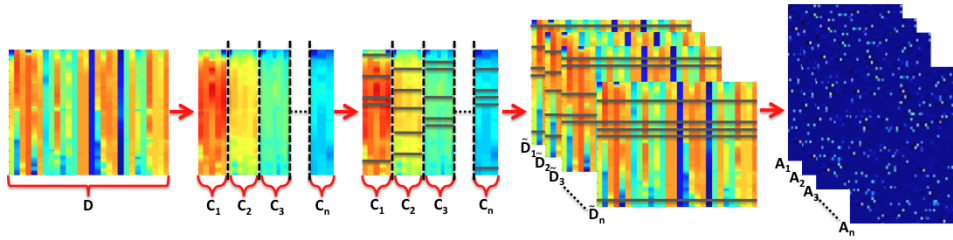


Figure 4: Illustration of computing ‘ n ’ sparse coefficient matrices with RCSC with a single library. The library is first clustered into ‘ n ’ clusters. Each cluster is then used to create a library \tilde{D}_i by removing the bands which have least variance in the cluster. With each library, a different sparse coefficient matrix A_i is computed.

affecting the spectral derivative’s ability of coherence reduction, we lower this sensitivity by using $c = 2$ in (9), which results in smoother differentiated spectra.

3. Proposed Solution

We propose two different algorithms for hyperspectral unmixing with constrained sparse coding. These algorithms are based on the following important observations. 1) For highly coherent spectral signatures, it is possible to reduce their mutual coherence by removing the bands from their spectra at which variance between the material reflectances is very low (see Fig. 3). 2) For spectral derivatives, adverse effects of noise on sparse unmixing can be mitigated by taking the spectral derivative such that it is not operated on the bands at which the material reflectances have very low variance across the spectral library. This happens because, at and near those bands, the highly coherent spectral signatures of materials are generally very similar to each other because of their inherent smooth nature [25]. Therefore, for noisy signals it is the noise that mainly contributes to the significant differences between the differentiated signals at those bands. Since, such differences can cause confusion in the unmixing process, we can simply neglect the aforementioned bands while taking the spectral derivative.

1. **Algorithm RCSC: Inputs \mathbf{D} , \mathbf{Y} returns \mathbf{A}**
2. **Sparse code:** Compute \mathbf{A}_0 with \mathbf{D} and \mathbf{Y} , using (7).
3. **Cluster:** Cluster the columns of \mathbf{D} into n clusters \mathbf{C}_i , s.t. $\mu(\mathbf{C}_i) \geq \cos \theta, \forall \mathbf{C}_i, i \in \{1, \dots, n\}$
4. *for each \mathbf{C}_i*
5. **Compute variance:** Compute variance of each row of \mathbf{C}_i
6. **Select rows:** Select ‘ f ’ fraction of rows with minimum variances.
7. **Remove bands:** Create $\tilde{\mathbf{D}}_i$ and $\tilde{\mathbf{Y}}_i$ by removing the rows corresponding to ‘ f ’ from \mathbf{D} and \mathbf{Y} .
8. **Sparse code:** Compute \mathbf{A}_i with $\tilde{\mathbf{D}}_i$ and $\tilde{\mathbf{Y}}_i$ using (7).
9. $\mathbf{A} = \frac{1}{2-f} \sum_{i=0}^n \beta_i \mathbf{A}_i$
10. return \mathbf{A}

Figure 5: Algorithm 1: Repeated-CSC (RCSC).

3.1. Repeated Constrained Sparse Coding (RCSC)

This method formulates hyperspectral unmixing as a constrained sparse coding problem and repeatedly solves the optimization function in Equation 7. The method is presented in Fig. 5 as an algorithm. RCSC first computes a sparse coefficient matrix \mathbf{A}_0 with the help of the given library \mathbf{D} and the HS image \mathbf{Y} (Fig. 5, line ‘2’). Later on, it computes ‘ n ’ different sparse coefficient matrices \mathbf{A}_i , where $i \in \{1, \dots, n\}$, such that an \mathbf{A}_i is computed with a library $\tilde{\mathbf{D}}_i$ and an image $\tilde{\mathbf{Y}}_i$ that are obtained by neglecting ‘ f ’ fraction of bands from \mathbf{D} and \mathbf{Y} , respectively. The algorithm uses all the intermediate sparse coefficient matrices to compute the final sparse coefficient matrix \mathbf{A} , whoes

columns represent the fractional abundances of the detected materials in the pixels of the HS image. Given a library \mathbf{D} and the image \mathbf{Y} , the bands that are neglected in computing an \mathbf{A}_i are selected as follows. The algorithm first clusters the spectral signatures in \mathbf{D} (Fig. 5, line '3'). Each cluster \mathbf{C}_i ($i \in \{1, \dots, n\}$) is created as an $m \times c$ matrix such that, $c > 2$ and $\mu(\mathbf{C}_i) \geq \cos \theta$, where θ denotes the threshold angle (i.e. the maximum angle allowed between any two spectral signatures in \mathbf{C}_i). For each \mathbf{C}_i , the algorithm selects ' f ' fraction of its rows with minimum variances. The rows corresponding to ' f ' are removed from \mathbf{D} and \mathbf{Y} to obtain $\hat{\mathbf{D}}_i$ and $\hat{\mathbf{Y}}_i$ (Fig. 5, line '7'). Since the rows of these matrices correspond to spectral bands, removing them simply means neglecting the corresponding spectral bands in the HS data. The algorithm computes a sparse coefficient matrix \mathbf{A}_i with the corresponding $\hat{\mathbf{D}}_i$ and $\hat{\mathbf{Y}}_i$ for each \mathbf{C}_i (Fig. 5, line '8'). It should be noticed that we use \mathbf{D} and \mathbf{Y} to compute \mathbf{A}_0 , but reduced matrices $\hat{\mathbf{D}}_i$ s and $\hat{\mathbf{Y}}_i$ s to compute all other \mathbf{A}_i s. This implies that all the learned sparse coefficient matrices may be different, however they have the same dimensions. After exhausting the list of the clusters, RCSC directly combines all the sparse coefficient matrices in a weighted fashion for calculating the final fractional abundance matrix \mathbf{A} (Fig. 5, line '9'), where:

$$\beta_i = \begin{cases} 1 & i = 0 \\ (1 - f)/n & i \neq 0 \end{cases}$$

There are two main advantages of solving (7) in a repeated manner as described above. 1) Each time when we drop spectral bands of the library, mutual coherence of highly similar spectral signatures belonging to the cluster under consideration, reduces. This improves \mathbf{A}_i if any of the constituent endmembers of the mixed pixels belongs to the cluster under consideration. 2) Even if none of the constituent endmembers belong to the current cluster, each time the sparse coding step converges to a slightly different sparse coefficient matrix. With our settings, each one of these matrices by itself achieves a reasonable endmember detection rate¹. Therefore, combining all the computed sparse coefficient matrices results in even better endmember detection.

3.2. Repeated Spectral Derivative (RSD)

This method uses the concept of spectral derivative (see section 2.3) and solves Equation 7 with an image $\hat{\mathbf{Y}}_i$ and a library $\hat{\mathbf{D}}_i$ to obtain a sparse coefficient matrix \mathbf{A}_i . This is repeated ' n ' times, such that each time $\hat{\mathbf{Y}}_i$ and $\hat{\mathbf{D}}_i$ represent different matrices which are obtained by taking spectral derivatives of \mathbf{Y} and \mathbf{D} . Each time the spectral derivative is taken such that it is operated on all the spectral bands

¹We make this observation based on the results of our further experiments not reported here.

1. **Algorithm RSD: Inputs \mathbf{D}, \mathbf{Y} returns \mathbf{A}**
2. **Cluster:** Cluster the columns of \mathbf{D} into n clusters \mathbf{C}_i ,
s.t. $\mu(\mathbf{C}_i) \geq \cos \theta, \forall \mathbf{C}_i, i \in \{1, \dots, n\}$
3. **for each \mathbf{C}_i**
4. **Compute variance:** Compute variance of each row of \mathbf{C}_i
5. **Select rows:** Select ' f ' fraction of rows with minimum variances.
6. **Differentiate:** Create $\hat{\mathbf{D}}_i = \Delta(\mathbf{D})$ and $\hat{\mathbf{Y}}_i = \Delta(\mathbf{Y})$ such that spectral derivative is not operated on bands corresponding to ' f '.
7. **Sparse code:** Compute \mathbf{A}_i with $\hat{\mathbf{D}}_i$ and $\hat{\mathbf{Y}}_i$ using (7).
8. $\mathbf{A} = \frac{1}{n} \sum_{i=1}^n \mathbf{A}_i$.
9. **return \mathbf{A}**

Figure 6: Algorithm 2: Repeated-Spectral Derivative (RSD).

in \mathbf{Y} and \mathbf{D} except at a small fraction ' f ' of them. As in RCSC, the value of ' n ' and the bands that correspond to ' f ' are found by clustering \mathbf{D} into ' n ' clusters stored in matrices \mathbf{C}_i ($i \in \{1, \dots, n\}$). Once again, the bands that belong to ' f ' are those which correspond to the rows of \mathbf{C}_i that have least variances. In $\hat{\mathbf{Y}}_i$ and $\hat{\mathbf{D}}_i$, the rows representing these bands are kept the same as those in \mathbf{Y} and \mathbf{D} . Since ' f ' represents a small fraction, it is also possible to simply drop these bands from the differentiated data and still achieve similar results. However, we prefer to use the original values of the reflectances at these bands to avoid any unnecessary loss of information.

Fig. 6 shows RSD as an algorithm. In this algorithm, after calculating the sparse coefficient matrices in each sparse coding step, the fractional abundance matrix \mathbf{A} is calculated as the weighted sum of all the sparse coefficient matrices. This weighted sum is simply the mean of the matrices because we give equal weight to each matrix, as each of them is calculated using the complete data.

4. Results and discussion

In this section, we present the results of applying the proposed methods to simulated data as well as real data acquired by the AVIRIS. In order to evaluate our methods we compare the results with the state of the art approach proposed in [3].

4.1. Spectral Library

We use the library of spectral signatures made publicly available by the NASA's Jet Propulsion Lab (<http://speclib.jpl.nasa.gov/>). This library, known as the ASTER spectral library [2], consists of spectra of 2400 materials of seven different types (e.g. minerals, rocks). In our experiments we take a subset of this library that consists of 500 materials which belong to type mineral, rock, soil and vegetation. This subset, \mathbf{D} (henceforth referred as the 'library') was created such that no two spectral signatures in it are more than 25 deg apart. Such a high mutual coherence between all the elements of the library is a rather

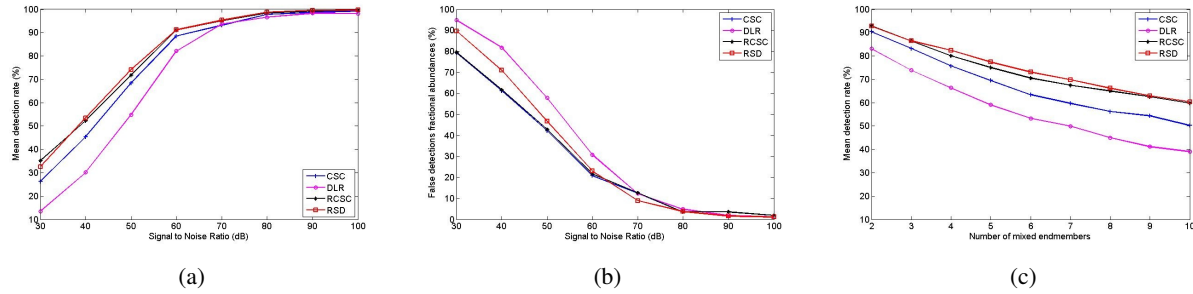


Figure 7: Comparison of the results of RCSC, RSD, CSC and DLR [3]. (a) Comparison of the mean endmember detection rate as a function of SNR (with $p = 5$). (b) Comparison of mean fractional abundances in false detections of endmembers with increasing SNR (with $p = 5$). (c) Comparison of the mean endmember detection rate as a function of cardinality of image pixels at 50 dB SNR.

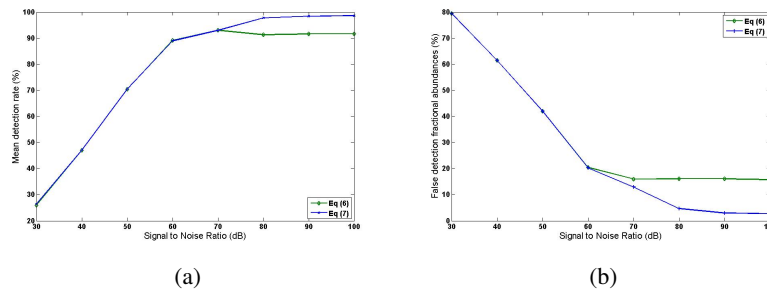


Figure 8: Comparison of optimization Equation 6, with $\eta = 10^{-6}$ and Equation 7, with $\lambda = 1.3$. (a) Compares the mean endmember detection rate as a function of SNR (with $p = 5$). (b) Shows mean fractional abundances in false detections of endmembers with increasing SNR (with $p = 5$).

strict condition. However, we impose this condition for better evaluation of the proposed methods, which aim at better performance even under such conditions. In all of the experiments we re-sample our library to 224 bands according to the AVIRIS data. That is, each reflectance spectra in the library is in the range $0.4 - 2.5\mu m$ sampled at $10nm$.

4.2. Simulated Data

We first test the proposed methods on simulated data, for which we create synthetic image cubes of dimensions $100 \times 100 \times 224$, where 224 is the spectral dimension. Each pixel of a synthetic HS cube is created by mixing ' p ' randomly selected signatures from the library. Values of fractional abundances associated with each spectra are also selected randomly such that the ASC holds for each pixel. After creation of a cube, we include additive white Gaussian noise. Each result presented below is the mean value calculated with ten synthetic HS cubes. In our experiments, we use $\lambda = 1.3$ in Equation 7. However, the results are relatively insensitive to the value of λ in the range $[1.1, 1.5]$. This range is based on ASC and allowing for any possible false detection of endmembers because of noise and high mutual coherence of the library. We select $\lambda = 1.3$ with

three fold cross-validation. Value of ' f ' in RCSC and RSD is kept at 0.1, whereas θ is chosen to be 7 deg.

Fig. 7 shows results of applying RCSC and RSD to the simulated data. The figure also includes results of applying the approach in [3] (shown as DLR in the figure) and directly performing CSC on the same data. For DLR, we use our own implementation which was done with the help of the authors of [3]. Fig. 7a shows the mean values of endmember detection rate as a function of SNR. Here, endmember detection rate is defined as the percentage of endmembers in a mixed pixel that have been correctly detected by an algorithm. The graph shows better endmember detection rates, especially at low SNR, for the proposed methods. When a sparse approximation method is used for hyperspectral unmixing, it can also result in false detections of endmembers. In order to properly evaluate a method, it is important to note the fractional abundances of the materials which have been falsely detected by the method. Fig. 7b shows the comparison of fractional abundances in the false detections (as percentage) for the methods, as a function of SNR. Here, curves for RCSC and RSD are similar to those of CSC and DLR respectively, which implies that both of the proposed methods are able to improve the endmem-

ber detection rate without significantly incurring false detections in the repetitions. In fact, for low SNR RSD outperforms DLR. This is because, while taking the spectral derivative RSD neglects the bands in the data that cause confusion in unmixing (see Fig. 6, line ‘6’). For RSD, fractional abundance in the false detections become almost zero beyond 110 dB, whereas they remain of the order of 3 for RCSC.

For a typical HS unmixing scenario in real images, the cardinality ‘ p ’ of a mixed pixel is generally of the order of five [14]. Therefore, the above mentioned results are evaluated with $p = 5$ for each pixel of each image. For different areas on land, the value of p can vary for different pixels. Fig. 7c shows the endmember detection rate for each method as a function of cardinality of the pixels of the images. Here, SNR is fixed at 50 dB. In the figure, the proposed methods clearly outperform CSC and DLR for all of the values of p . Notice that, the results for CSC, RCSC and RSD shown in Fig. 7 are obtained under our settings. That is, for each of these methods we solve for Equation 7 with $\lambda = 1.3$, while performing sparse coding. On the other hand, the results for DLR are obtained by solving for Equation 6, with $\eta = 10^{-6}$ as in [3]². It is interesting to know the effects of formulating the sparse coding problem as Equation 7 instead of Equation 6. For both of these equations, Fig. 8 shows the endmember detection rate (Fig. 8a) and the fractional abundance in false detections (Fig. 8b) as a function of SNR. In the figure, there is a clear separation between the curves at high SNR. The main reason behind this separation is that Equation 6 minimizes the l_1 norm of the coefficient vector without any explicit bounds on it. This limits its performance at high SNR where high mutual coherence between the pure spectral signatures result in false detection of similar endmembers within the tolerance allowed for the reconstruction error. On the other hand, Equation 7 explicitly constraints the l_1 norm of the coefficient vector through λ , which is justified by ASC. Thus, minimizing the reconstruction errors without explicit lower bounds result in a better performance at high SNR.

4.3. Real Data

We apply RCSC and RSD on the real HS image collected by AVIRIS (http://aviris.jpl.nasa.gov/data/free_data.html). From this image, we selected an HS cube of dimension $614 \times 512 \times 224$. The spatial dimensions (614×512) of this cube represent a region of Cuprite mines, Nevada which has been well studied in Geological Sciences literature for its surface materials. Fig. 9a shows material classification results of this region from [9] which are generally used as a benchmark for qualitative evaluation of hyperspectral unmixing approaches in remote sensing community. To apply our methods to real data, we first drop 24 spectral bands

²Under our settings results of DLR are worse than those reported here.

in the HS cube (and the library) that have zero or very low values of reflectance due to atmospheric absorptions. Furthermore, we rely on advanced atmospheric correction algorithms to convert the at-sensor radiance measurement by AVIRIS to reflectance units in order to match spectral signatures in the used library, which are measured in laboratory conditions. These algorithms have already been applied to the available image.

Fig. 9b shows the abundance maps created by RSD (left) and RCSC (right) of a material ‘K-Alunite’ present in the region. The region shown in the figure corresponds to the region magnified in Fig. 9a. As can be seen in the abundance maps, most of the ‘K-Alunite’ has been correctly identified by both of the methods. However, results of RSD are better in the sense that the algorithm does not over estimate the presence of ‘K-Alunite’. This is the consequence of coherence reduction with spectral derivative. RCSC incorrectly detects ‘K-Alunite’ at some regions where the materials with similar spectral signatures are present. For instance, it also detects ‘K-Alunite’ in some regions which have been classified as ‘Alunite+Kaolinite and/or Muscovite’ and ‘Kaolinite’ according to [9].

5. Conclusion

In this work, we formulate hyperspectral unmixing as a constrained sparse coding problem and propose two different methods to achieve high endmember detection rates, especially with low SNR of HS images. Both of the methods solve for constrained sparse coding optimization function in a repeated manner. In the first method, called RCSC, we systematically remove a small fraction of spectral bands from the data each time before computing a sparse coefficient matrix. The final fractional abundance matrix is then computed as a weighted sum of all the computed sparse coefficient matrices. In the second method, called RSD, we make use of spectral derivative, which is operated on all the bands of the data except a small fraction of them. After sparse coding with the differentiated data each time, we calculate the fractional abundance matrix as the mean of the sparse coefficient matrices obtained in each sparse coding step. We apply the methods to both simulated as well as real HS images. We compare the results of hyperspectral unmixing with a state of the art approach proposed in [3]. Results show better performance of the proposed methods, especially at low SNR of HS images.

References

- [1] Environmental mapping and analysis program, <http://www.enmap.org/>, March 2013. 1
- [2] A. M. Baldridge, S. Hook, C. Grove, and G. Rivera. The aster spectral library version 2.0. *remote sensing of environment. Remote Sensing of Environment*, 113:711–715, 2009. 2, 5

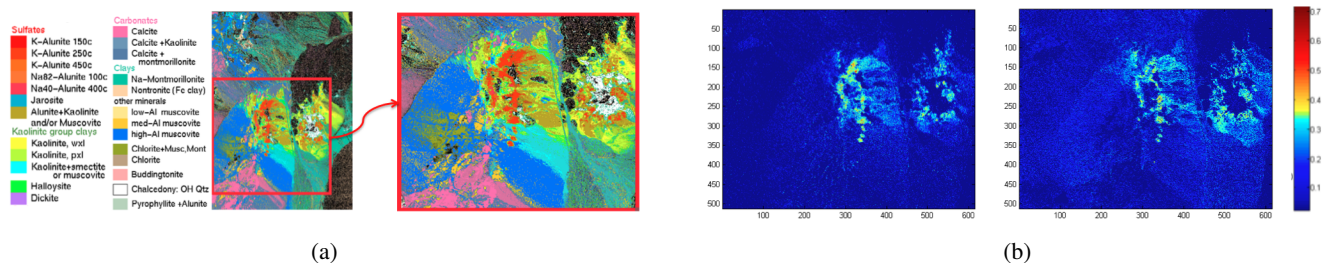


Figure 9: Results on real data: (a) Classification results of Cuprite mines, Nevada from [9]. To evaluate the proposed approaches we use the HS cube taken over the region magnified in the image. (b) Abundance maps for K-Alunite created by RSD (left) and RCSC (right) for the region magnified in Fig. 9a.

- [3] J. Bieniarz, R. Mueller, X. Zhu, and P. Reinartz. On the use of overcomplete dictionaries for spectral unmixing. In *4th Workshop on Hyperspectral Image and Signal Processing: Evolution in Remote Sensing*, 2012. 1, 2, 3, 5, 6, 7
- [4] J. Bieniarz, R. Mueller, X. Zhu, and P. Reinartz. Sparse approximation, coherence and use of derivatives in hyperspectral unmixing. In *Third Annual Hyperspectral Imaging Conference, Rome, Italy*, 2012. 1, 2, 3
- [5] J. M. Bioucas-Dias, A. Plaza, N. Dobigeon, M. Parente, Q. Du, and P. Gader. Hyperspectral unmixing overview: Geometrical, statistical, and sparse regression-based approaches. *IEEE Journal of Selected Topics in Applied Earth Observations and Remote Sensing*, 2012. 1, 2
- [6] J. W. Boardman, F. A. Kruse, and R. O. Green. Mapping target signatures via partial unmixing of aviris data. In *JPL Airborne Earth Sci. Workshop*, pages 23–26, 1995. 2
- [7] S. S. Chen, D. L. Donoho, Michael, and A. Saunders. Atomic decomposition by basis pursuit. *SIAM Journal on Scientific Computing*, 20:33–61, 1998. 3
- [8] R. N. Clark, G. A., K. E. Swayze, R. F. Livo, S. J. Kokaly, J. B. Sutley, R. R. Dalton, McDougal, and C. A. Gent. Imaging spectroscopy: Earth and planetary remote sensing with the usgs tetra-corder and expert systems. *Journal of Geophysical Research*, 2003. 2
- [9] R. N. Clark, G. A., K. E. Swayze, R. F. Livo, S. J. Kokaly, J. B. Sutley, R. R. Dalton, McDougal, and C. A. Gent. Imaging spectroscopy: Earth and planetary remote sensing with the usgs tetra-corder and expert systems. *Journal of Geophysical Research*, 2003. 7, 8
- [10] R. Green, M. L. Eastwood, C. M. Sarture, T. G. Chrien, M. Aronsson, B. J. Chippendale, J. A. Faust, B. E. Pavri, C. J. Chovit, M. Soils, M. R. Olah, and O. Williams. Imaging spectroscopy and the airborne visible/infrared imaging spectrometer (aviris). *Remote Sensing of Environment*, 65(3):227–248, 1998. 1
- [11] A. Farraguerra and C.-I. Chang. Multispectral and hyperspectral image analysis with convex cones. *IEEE Trans. Geosci. Remote Sens.*, 37(2):756–770, 1999. 2
- [12] M. Iordache. *A sparse regression approach to hyperspectral unmixing*. PhD thesis, Universidade Tecnica de Lisboa, Instituto Superior Tecnico, Nov 2011. 2
- [13] M. D. Iordache, J. Bioucas-Dias, and A. Plaza. On the use of spectral libraries to perform sparse unmixing of hyperspectral data. In *IEEE GRSS Workshop Hyperspectral Image Signal Process.: Evolution in Remote Sens.*, 2010. 2
- [14] M.-D. Iordache, J. Bioucas-Dias, and A. Plaza. Sparse unmixing of hyperspectral data. *Geoscience and Remote Sensing, IEEE Transactions on*, 49(6):2014–2039, 2011. 1, 2, 3, 7
- [15] J. Li and J. M. Bioucas-Dias. Minimum volume simplex analysis: A fast algorithm to unmix hyperspectral data. In *Geoscience and Remote Sensing Symposium*, 2008. 2
- [16] L. Miao and H. Qi. Endmember extraction from highly mixed data using minimum volume constrained nonnegative matrix factorization. *IEEE Trans. Geosci. Remote Sens.*, 45(3):765–777, March 2007. 2
- [17] NASA. Earth observatory, <http://earthobservatory.nasa.gov/>, July 2013. 1
- [18] J. M. P. Nascimento and J. M. Bioucas-Dias. Vertex component analysis: A fast algorithm to unmix hyperspectral data. *IEEE Trans. Geosci. Remote Sens.*, 2005. 1
- [19] R. A. Neville, K. Staenz, T. Szeredi, J. Lefebvre, and P. Hauff. Automatic endmember extraction from hyperspectral data for mineral exploration. In *21st Can. Symp. Remote Sens.*, pages 21–24, 1999. 2
- [20] A. Plaza and C.-I. Chang. Impact of initialization on design of endmember extraction algorithms. *IEEE Trans. Geosci. Remote Sens.*, 44(11):3397–3407, November 2006. 1
- [21] A. Plaza, P. Martinez, R. Perez, and J. Plaza. A quantitative and comparative analysis of endmember extraction algorithms from hyperspectral data. *IEEE Trans. Geosci. Remote Sens.*, 42(3):650–663, March 2004. 1
- [22] H. Ren and C.-I. Chang. Automatic spectral target recognition in hyperspectral imagery. *IEEE Trans. Aerosp. Electron. Syst.*, 39(4):1232–1249, 2003. 2
- [23] R. Tibshirani. Regression shrinkage and selection via the lasso. *Journal of the Royal Statistical Society, Series B*, 58:267–288, 1994. 3
- [24] M. E. Winter. N-finder: An algorithm for fast autonomous spectral end-member determination in hyperspectral data. In *SPIE Imaging Spectrometry V*, 2003. 2
- [25] Z. Xing, M. Zhou, A. Castrodad, G. Sapiro, and L. Carin. Dictionary Learning for Noisy and Incomplete Hyperspectral Images. *SIAM Journal on Imaging Sciences*, 5(1):33–56, 2012. 4